Lecture Notes in Electrical Engineering 1176

Yi Qu
Mancang Gu
Yifeng Niu
Wenxing Fu *Editors*

Proceedings of 3rd 2023 International Conference on Autonomous Unmanned Systems (3rd ICAUS 2023)

Volume VI

Springer

Lecture Notes in Electrical Engineering 1176

Series Editors

The book series *Lecture Notes in Electrical Engineering* (LNEE) publishes the latest developments in Electrical Engineering—quickly, informally and in high quality. While original research reported in proceedings and monographs has traditionally formed the core of LNEE, we also encourage authors to submit books devoted to supporting student education and professional training in the various fields and applications areas of electrical engineering. The series cover classical and emerging topics concerning:

- Communication Engineering, Information Theory and Networks
- Electronics Engineering and Microelectronics
- Signal, Image and Speech Processing
- Wireless and Mobile Communication
- Circuits and Systems
- Energy Systems, Power Electronics and Electrical Machines
- Electro-optical Engineering
- Instrumentation Engineering
- Avionics Engineering
- Control Systems
- Internet-of-Things and Cybersecurity
- Biomedical Devices, MEMS and NEMS

For general information about this book series, comments or suggestions, please contact leontina.dicecco@springer.com.

To submit a proposal or request further information, please contact the Publishing Editor in your country:

China

Jasmine Dou, Editor (jasmine.dou@springer.com)

India, Japan, Rest of Asia

Swati Meherishi, Editorial Director (Swati.Meherishi@springer.com)

Southeast Asia, Australia, New Zealand

Ramesh Nath Premnath, Editor (ramesh.premnath@springernature.com)

USA, Canada

Michael Luby, Senior Editor (michael.luby@springer.com)

All other Countries

Leontina Di Cecco, Senior Editor (leontina.dicecco@springer.com)

**** This series is indexed by EI Compendex and Scopus databases. ****

Yi Qu · Mancang Gu · Yifeng Niu · Wenxing Fu
Editors

Proceedings of 3rd 2023 International Conference on Autonomous Unmanned Systems (3rd ICAUS 2023)

Volume VI

Springer

Editors
Yi Qu
Nanjing University of Science
and Technology
Nanjing, China

Mancang Gu
Beijing HIWING Scientific
and Technological Information Institute
Beijing, China

Yifeng Niu
College of Intelligence Science
and Technology
National University of Defense Technology
Changsha, Hunan, China

Wenxing Fu
Unmanned System Research Institute
Northwestern Polytechnical University
Xi'an, Shaanxi, China

ISSN 1876-1100 ISSN 1876-1119 (electronic)
Lecture Notes in Electrical Engineering
ISBN 978-981-97-1098-0 ISBN 978-981-97-1099-7 (eBook)
https://doi.org/10.1007/978-981-97-1099-7

This Springer imprint is published by the registered company Springer Nature Singapore Pte Ltd.
The registered company address is: 152 Beach Road, #21-01/04 Gateway East, Singapore 189721, Singapore

Paper in this product is recyclable.

Contents

Improved Factor Graph Algorithm for Adaptive Weight Function Based on Residual Adjustment

Congcong Wang, Rong Wang(✉), Jingxin Zhao, Zhi Xiong, and Jianye Liu

Navigation Research Center, College of Automation Engineering, Nanjing University of Aeronautics and Astronautics, Nanjing 211106, China
rongwang@nuaa.edu.cn

Abstract. To address the issue of traditional factor graph methods being unable to handle the dynamic change in sensor measurement accuracy during the operational process, an adaptive weight function is introduced and an improved factor graph method based on adaptive weight is proposed. By calculating the residual between the predicted value of inertial preintegration and the measured value of auxiliary sensors in real-time, the fusion information weight of the corresponding factor nodes are dynamically adjusted. Compared with traditional factor graph algorithms, this method can improve the optimization accuracy and robustness of factor graph algorithms in the situation of step faults, gradual faults, or rejection faults in auxiliary sensors. The simulation experimental results show that when the auxiliary sensor produces measurement faults, compared with traditional factor graph method, the improved factor graph method based on adaptive weights has higher robustness and accuracy. When measurement faults occur in auxiliary sensors, its position, velocity, and attitude estimation accuracy RMSE values have been improved by more than 45%.

Keywords: Residual adjustment · Adaptive weight function · Kernel function · Factor graph

1 Introduction

With the development of modern navigation technology and sensor hardware technology, inertial navigation system (INS) has been widely used in various navigation fields such as unmanned aerial vehicles, autonomous underwater vehicles, and unmanned vehicles due to its characteristics of autonomy, concealment, low cost, and small size [1, 2]. However, the navigation error of INS will gradually diverge over time.

In 2012, based on the "All Source Positioning and Navigation" (ASPN) [3] concepts and the factor graph method proposed by Kschis [4], Indelman introduced the factor graph structure into inertial integrated navigation, and proved the factor graph method has an advantage in accuracy when solving nonlinear problems in navigation systems that compared to traditional filtering methods [5]. For factor graph algorithms, the error model corresponding to sensor measurement factors is crucial for solving navigation state variables. Previous noise models typically relied on empirical or statistical experimental

Y. Qu et al. (Eds.): ICAUS 2023, LNEE 1176, pp. 1–10, 2024.
https://doi.org/10.1007/978-981-97-1099-7_1

methods. However, in practical scenarios, the error model is usually not fixed, and the measurement data of sensors may generate measurement errors due to internal or external reasons. In this case, a noise model based on experience often cannot obtain the optimal estimation [6].

In response to the problem of setting the noise model for the factor graph mentioned above, some scholars have studied estimation methods based on adaptive covariance. David improved estimation accuracy by estimating the covariance during the 3D point cloud registration process, but this method heavily relies on the quality of input information [7]. Based on the theory of David, Zixu Zhao introduced the maximum expectation algorithm to achieve benchmark free adaptive covariance estimation [8]. The above methods are all based on methods in visual images, but reference [9] proposed an adaptive factor graph method based on sliding windows, which estimates the covariance matrix by calculating the residuals within the sliding window. However, this method requires the calculation of measurement data within a certain sliding window, which is computationally expensive.

By summarizing the literature, current Factor graph algorithm still needs to solve the problem of dynamic change of sensor accuracy during movement. Based on the background, this paper proposes an improved Factor graph algorithm (AFG) based on adaptive weight function. The contribution of this paper is:

1. This article designs an adaptive weight function to handle the dynamic change in sensor accuracy during motion in real-time. Specifically, the concept of Gaussian kernel function is introduced in the adaptive weight function, and the kernel width is used to achieve adaptively adjust the fusion weight of factor nodes.
2. By using the adaptive weight function, the AFG algorithm can has more robust in the face of sensor faults of step, slow, and rejection.

2 Factor Graph Model

The first step of factor graph fusion algorithm requires to construct corresponding sensor factor model. This chapter derives the factor formula for the sensor measurement model of the vehicle integrated navigation system for INS, GNSS, LIDAR, Odemetry (OD) and Magnetometer (MAG).

2.1 INS Preintegrated Factor Model

In order to facilitate the plug and play of various navigation sensors in the factor graph structure and reduce the update frequency of the factor graph, this article uses the preintegrated method to construct the factor nodes of the INS [10].

According to the INS preintegrated method, its process can be expressed as the following state equation after discretization, between t_k and t_{k+1}:

$$\tilde{\mathbf{x}}_{k+1}^{\mathrm{INS}} = h\left(\mathbf{x}_k, \boldsymbol{\alpha}_k, \mathbf{z}_k^{\mathrm{INS}}\right) \tag{1}$$

where $\mathbf{x}_k$ represents the position, velocity, and attitude of the INS in the navigation coordinate system, $\boldsymbol{\alpha}_k$ represents the deviation correction of the accelerometer and gyroscope, $\mathbf{z}_k^{\mathrm{INS}}$ is the measurement value of INS. $\tilde{\mathbf{x}}_{k+1}^{\mathrm{INS}}$ is the predicted navigation state.

The INS factor node is defined as the error between the predicted value at the time t_{k+1} and the current estimated value $\hat{\mathbf{x}}_{k+1}$, the INS factor can be defined as Eq. (2), where $d(\cdot)$ represents the cost function.

$$f^{\mathrm{INS}}(\mathbf{x}_{k+1}, \mathbf{x}_k, \boldsymbol{\alpha}_k) = d\left(\hat{\mathbf{x}}_{k+1} - h\left(\mathbf{x}_k, \boldsymbol{\alpha}_k, \mathbf{z}_k^{\mathrm{INS}}\right)\right) \tag{2}$$

In this paper, the deviation correction of accelerometer and gyroscope is described by nonlinear random walk model:

$$\tilde{\alpha}_{k+1} = c(\boldsymbol{\alpha}_k) \tag{3}$$

where $c(\bullet)$ represents the nonlinear function of deviation correction. In addition, due to the divergent characteristics of INS, after each preintegrated, it is necessary to correct the deviation. Similarly, the INS deviation factor can be defined as follows, $\boldsymbol{\alpha}_{k+1}$ represents the deviation correction at time t_{k+1}.

$$f^{\mathrm{bias}}(\boldsymbol{\alpha}_{k+1}, \boldsymbol{\alpha}_k) = d(\boldsymbol{\alpha}_{k+1} - c(\boldsymbol{\alpha}_k)) \tag{4}$$

2.2 GNSS, LIDAR, OD, and MAG Factor Model

In the paper, GNSS is used to provide position, velocity, and attitude information of the carrier in the navigation system, usually the measurement equation of GNSS can be defined as:

$$\mathbf{z}_k^{\mathrm{GNSS}} = h^{\mathrm{GNSS}}(\mathbf{x}_k) + \boldsymbol{\eta}^{\mathrm{GNSS}} \tag{5}$$

where $\mathbf{x}_k$ represents the position, velocity, and attitude measurement information of GNSS, $\boldsymbol{\eta}^{\mathrm{GNSS}}$ represents the measurement noise of the corresponding state variable, and $h^{\mathrm{GNSS}}(\bullet)$ represents the relationship between the current navigation state of the carrier and $\mathbf{z}_k^{\mathrm{GNSS}}$. The GNSS factor node can be defined as:

$$f^{\mathrm{GNSS}}\left(\mathbf{x}_k, \mathbf{z}_k^{\mathrm{GNSS}}\right) = d\left(\mathbf{z}_k^{\mathrm{GNSS}} - h^{\mathrm{GNSS}}(\mathbf{x}_k)\right) \tag{6}$$

Similar to GNSS, LIDAR, OD and MAG factors can be defined as:

$$f^{\mathrm{LIDAR}}\left(\mathbf{x}_k, \mathbf{z}_k^{\mathrm{LIDAR}}\right) = d\left(\mathbf{z}_k^{\mathrm{LIDAR}} - h^{\mathrm{LIDAR}}(\mathbf{x}_k)\right) \tag{7}$$

$$f^{\mathrm{OD}}\left(\mathbf{x}_k, \mathbf{z}_k^{\mathrm{OD}}\right) = d\left(\mathbf{z}_k^{\mathrm{OD}} - h^{\mathrm{OD}}(\mathbf{x}_k)\right) \tag{8}$$

$$f^{\mathrm{MAG}}\left(\mathbf{x}_k, \mathbf{z}_k^{\mathrm{MAG}}\right) = d\left(\mathbf{z}_k^{\mathrm{MAG}} - h^{\mathrm{MAG}}(\mathbf{x}_k)\right) \tag{9}$$

After building the models, the factor graph model is shown in Fig. 1, in which f_x^{prior} and $f_\alpha^{\mathrm{prior}}$ are the factor nodes of prior information of navigation state variables and INS deviation variables, respectively. The auxiliary sensor receives real time measurement information of GNSS, LIDAR, OD, and MAG.

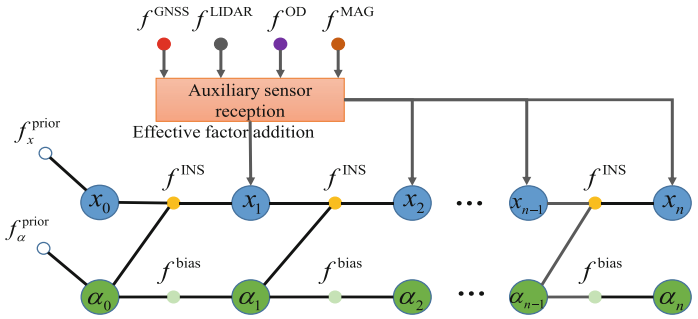

Fig. 1. Multi-source navigation sensor fusion factor graph model

3 Improved Factor Graph Based on Adaptive Weights

Based on the construction of the sensor factor model in the previous chapter, this chapter sets adaptive weight functions through the kernel function [11] and proposes an improved factor graph algorithm based on adaptive weight. The basic process is shown in Fig. 2. This algorithm is based on a loosely coupled structure, calculates the kernel width in real-time through the residual. Afterwards, the fusion weight of the auxiliary sensor factor nodes is adjusted through adaptive weight functions.

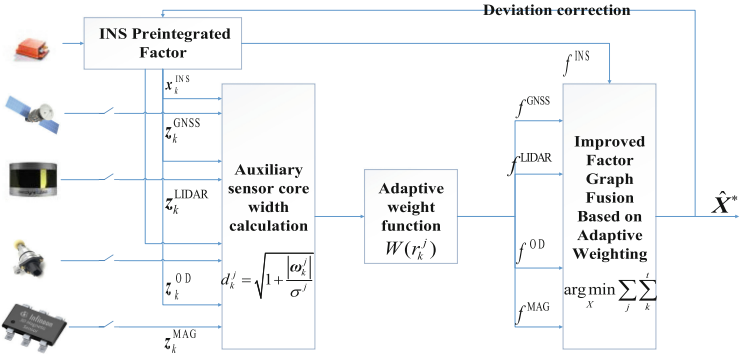

Fig. 2. Complete process of improved factor graph algorithm based on adaptive weights

3.1 Principle of Adaptive Weight Factor Graph

The adaptive weight function dynamically adjusts the information weights of each factor node based on the residual of auxiliary sensor measurement information. Before adding new measurement value to the factor graph structure, the adaptive weight function is used to distinguish and calculate: when the measurement information is considered abnormal, the corresponding factor node weight value will decrease; When the new measurement value is considered normal, the corresponding node weight will increase.

Based on the description of the above method, the adaptive weight function $W(r_k^j)$ at time k as follows,$j \in \{\text{GNSS, LIDAR, OD, MAG}\}$ means the types of auxiliary sensors.

$$W(r_k^i) = \begin{cases} 1, & 0 \le r_k^j \le \tau_1^j \\ \exp\left(-\frac{\left\|r_k^j - \tau_1^j\right\|^2}{2(d_k^j)^2}\right), & 0 < r_k^j < \tau_1^j \end{cases} \tag{10}$$

where d_k^j is the kernel width of the Gaussian kernel function corresponding to the auxiliary sensor at time k, τ_1^j is the threshold of auxiliary sensors, r_k^j is the modulus of the residual matrix between the predicted INS value and the measured value of the auxiliary sensor j. The trend of weight change under different kernel widths are shown in Fig. 3. As shown in Fig. 4, Different sensors have different kernel widths, and their adaptive weight functions have different slopes.

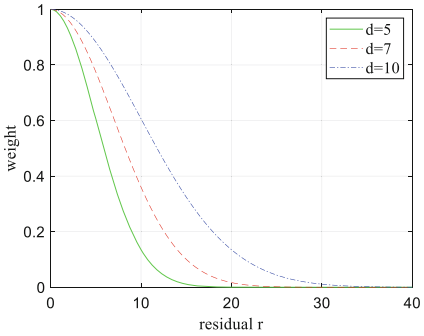

Fig. 3. Trend of weight changes under different kernel widths

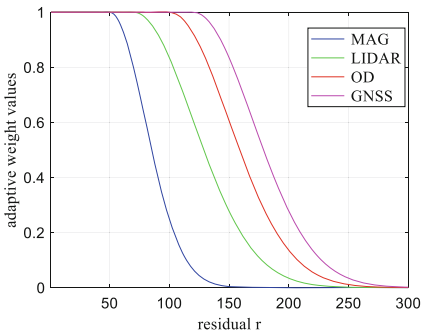

Fig. 4. Slope of adaptive weight function for each sensor under different kernel widths

The above function adjusts the information weight of factor nodes. Modifying the information weight in the factor graph is equivalent to multiply the adaptive weight function in cost function during factor graph optimization. The new cost function is:

$$\hat{X}^* = \arg\min_X \left(\sum_{k=0}^{t} ||h(\boldsymbol{x}_k, \boldsymbol{a}_k, \boldsymbol{z}_k^{\text{INS}}) - \hat{\boldsymbol{x}}_{k+1}||^2_{\sum_k} + \sum_j \sum_{k=0}^{t} ||W(r_k^j) \bullet (h_j(\boldsymbol{x}_k) - \boldsymbol{z}_k^j)||^2_{\sum_k^j} \right) \tag{11}$$

Obviously, for different types of auxiliary sensors, the adaptive weight function $W(\bullet)$ will vary, mainly reflected in the residual threshold r_1^j and kernel function width d_k^j. Due to the different working modes and measurement accuracy of each sensor, different residual thresholds and kernel width can be set separately.

According to the definition of residual r_k^j, its probability density function satisfies the χ distribution after normalization. It defines the credible range of measurement information. To ensure that the statistical significance and the credible probability are not too small, it is necessary to set between the maximum probability value and the average value of the χ distribution [12].

3.2 Auxiliary Sensor Kernel Width and Threshold

At time t_k, the residual between the measured value $\mathbf{z}_k^j$ of the auxiliary sensor j and the INS prediction value[13] is:

$$\bar{\boldsymbol{V}}_k^j = \boldsymbol{H}_k \tilde{\boldsymbol{x}}_k^{\mathrm{INS}} - \boldsymbol{z}_k^j \tag{12}$$

where $\mathbf{H}_k$ is the coefficient matrix of the measurement equation. So the prediction residual statistic is constructed from the above prediction residual:

$$\Delta \overline{\boldsymbol{V}}_k^j = \left(\frac{\overline{\boldsymbol{V}}_k^{jT} \bullet \overline{\boldsymbol{V}}_k^j}{\mathrm{tr}(\sum_{\overline{\boldsymbol{V}}_k^j})} \right)^{\frac{1}{2}} \tag{13}$$

where tr(•) is the trace of matrix, $\sum$ is the covariance matrix of corresponding matrix. The residual of the adaptive weight function is the modulus of the Eq. (13):

$$r_k^j = \left| \Delta \overline{\mathbf{V}}_k^j \right| \tag{14}$$

For the threshold τ_1^j, the value of the corresponding auxiliary sensor is between 1 and 2.5. The width of the Gaussian kernel function corresponding to the sensor measurement value at time k can be defined as:

$$d_k^j = \sqrt{1 + \frac{\left| \boldsymbol{\omega}_k^j \right|}{\sigma^j}} \tag{15}$$

where σ^j is the proportion coefficient of the corresponding sensor, selected based on experience, $\boldsymbol{\omega}_k^j$ is the standardized residual between the auxiliary sensor measurement value and the INS predicted value at time k, namely:

$$\boldsymbol{\omega}_k^j = \frac{\Delta \overline{\boldsymbol{V}}_k^j}{\boldsymbol{\beta}_k^j} \tag{16}$$

In the Eq. (16), $\boldsymbol{\beta}_k^j$ is the residual standard deviation.

4 Experiment

This section uses simulation experiment to build an INS/GNSS/LIDAR/OD/MAG integrated navigation system in an on-board environment to verify the effectiveness of the proposed improved factor graph algorithm.

4.1 Simulation Track Settings

Assuming an autonomous vehicle travels at an initial heading angle 90°, initial longitude $\lambda = 118°$, initial latitude $L = 32°$, initial altitude $h = 0$m, and simulation duration of 600 s. The simulation parameter settings for INS: Gyroscope bias is 0.02°/h, Gyroscope noise is 0.01°/h, Accelerometer bias is $1e^{-4}$*g, Accelerometer noise is $5e^{-5}$*g, and frequency is 100 Hz. In addition, in the experiment, the position error of GNSS is 10m, the velocity error is 1m/s, the attitude error is 0.03°, the position error of LIDAR is 6m, the velocity error of odometer is 0.4m/s, the attitude error of MAG is 0.01°, and their frequency are 2 Hz.

4.2 Multi-sensor Fault Adaptation Experiment

This section sets GNSS occurs a step fault of 50m, 5m/s, 3° between 200–230 s, and rejection fault between 270–320 s; LIDAR occurs a slow change fault of 5m/s between 15–35 s and rejection fault between 310–360 s; OD occurs a slow change fault of 0.5m/s^2 in 45–65 s, and rejection fault in 350–400 s; MAG occurs a slow change fault of 0.3°/s between 150–170 s and rejection fault between 380–430 s. The proportion coefficient in Eq. (15) are $\sigma^{\mathrm{GNSS}} = 0.1, \sigma^{\mathrm{LIDAR}} = 0.06, \sigma^{\mathrm{OD}} = 0.04, \sigma^{\mathrm{MAG}} = 0.01$. The optimization result of the traditional factor graph method (FG) and our algorithm (AFG) is shown in Figs. 5, 6 and 7, and the root mean square errors are shown in Table 1.

From the Fig. 5, compared with FG, the AFG algorithm can effectively handle both the step and slow change fault of position. According to Fig. 6, the AFG also can solve the velocity fault problem that occurs whether step or slow change. In Fig. 7, compared to traditional Factor graph, our algorithm also has a good effect on attitude fault, and its effect is more pronounced than position and speed. Benefiting by the plug and play structure of the Factor graph, two algorithms show the same effect in the face of rejection failure.

Figure 8 shows the curve of the adaptive weight values over time corresponding to the failure of the auxiliary sensor. From the figure, the adaptive weight function can flexibly adjusts the weight value of the corresponding node to achieve the AFG algorithm of this paper, whether it is measuring faults such as step and slow change, or rejecting faults.

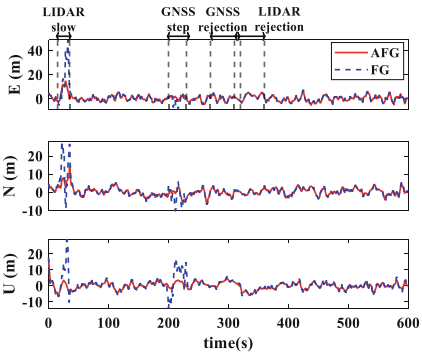

Fig. 5. Position estimation error in the ENU coordinate system

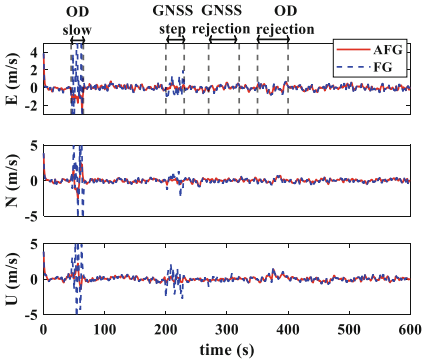

Fig. 6. Velocity estimation error in ENU coordinate system

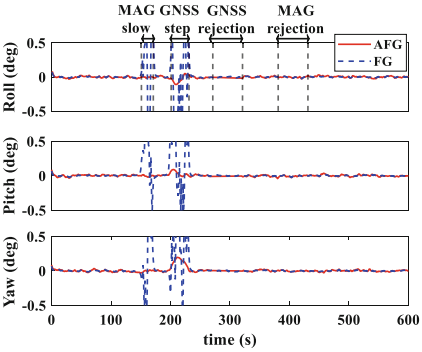

Fig. 7. Attitude estimation error in navigation system

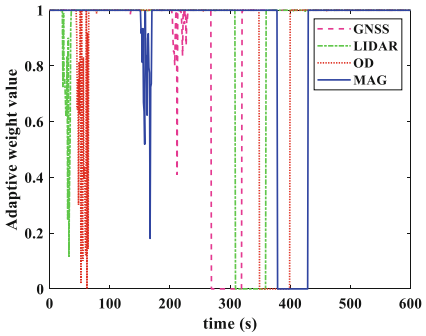

Fig. 8. Curve of auxiliary sensor adaptive weight function over time

From Table 1, it can be seen that compared with the traditional factor graph algorithm, the AFG algorithm has increased the RMSE of the position, velocity in ENU coordinate system, and attitude in navigation coordinate system by more than 45.0%, 52.6%, and 88.5%, respectively. Because of the fact that the accuracy of attitude angles is generally higher than position and velocity, and the attitude error in measurement information is the largest, so the accuracy improvement of attitude angles are also the greatest. This data verify the effectiveness of the AFG algorithm for sensor fault of step fault, slow change fault and reject fault.

Table 1. Three Methods for Estimating RMSE Values of State Variables

State	Type	FG	AFG
Position error (m)	East	4.84	2.63
	North	3.74	2.26
	Up	4.24	2.20
	Position	4.30	2.37
Velocity error (m/s)	East	0.76	0.36
	North	0.80	0.37
	Up	0.78	0.36
	Velocity	0.78	0.37
Attitude error (deg)	Roll	0.236	0.019
	Pitch	0.208	0.016
	Yaw	0.175	0.034
	Attitude	0.208	0.024

5 Conclusion

In order to overcome the problem that the traditional Factor graph algorithm cannot solve the dynamic change of sensor accuracy. This article proposes an improved Factor graph algorithm for improving fusion accuracy. A model containing INS, GNSS, LIDAR, OD, MAG integrated navigation factor graph is established, and an adaptive weight function is designed based on above. The advantage of this algorithm is that it can significantly improve the fusion accuracy of the Factor graph algorithm when the sensor fails, but the disadvantage is that when the actual sensor output is asynchronous, it is difficult to accurately use the INS prediction value to compare with the auxiliary sensor measurement value. The method in this paper broadens the application of Factor graph to sensor failure in integrated navigation. In the future, Factor graph can be used for long-term navigation, such as autonomous underwater vehicles and unmanned aerial vehicles. Their environment is more harsh, and the interference will be more complex and changeable. Therefore, the research on robustness of Factor graph algorithm will be the focus of further development in the future.

Acknowledgements. This work was partially supported by the National Natural Science Foundation of China (Grant No. 62073163, 61703208, 61873125), the Fundamental Research Funds for the Central Universities (Grant No. NT2022009, NZ2020004, NZ2019007), “Qing Lan Project” of Jiangsu Province, the Science and Technology Innovation Project for the Selected Returned Overseas Chinese Scholars in Nanjing, the Shanghai Aerospace Science and Technology Innovation Fund(SAST2020–073, SAST2019–085), the Foundation of Key Laboratory of Navigation, Guidance and Health-Management Technologies of Advanced Aircraft (Nanjing University of Aeronautics and Astronautics),Ministry of Industry and Information Technology, the Foundation of Engineering Research Center of Autonomous Control Technology of Aircraft (Nanjing University of Aeronautics and Astronautics), Ministry of Education, Jiangsu Key Laboratory “Internet

of Things and Control Technologies" & the Priority Academic Program Development of Jiangsu Higher Education Institutions.

References

1. Zhang, G., Hsu, L.T.: Intelligent GNSS/INS integrated navigation system for a commercial UAV flight control system. Aerosp. Sci. Technol. **80**, 363–380 (2018)
2. Kwak, J., Sung, Y.: Autonomous UAV flight control for GPS-based navigation. IEEE Access **6**, 37947–37955 (2018)
3. Granados, J.Á.F., Batalla, J.M., Togay, C.: Redundant localization system for automatic vehicles. Mech. Syst. Signal Process. **136**, 106433 (2020)
4. Kschischang, F.R., Frey, B.J., Loeliger, H.A.: Factor graphs and the sum-product algorithm. IEEE Trans. Inf. Theory **47**(2), 498–519 (2001)
5. Indelman, V., et al.: Factor graph based incremental smoothing in inertial navigation systems. In: 2012 15th International Conference on Information Fusion, pp. 2154–2161. IEEE, Singapore (2012)
6. Zhao, W., et al.: A novel Factor graph and cubature Kalman filter integrated algorithm for single-transponder-aided cooperative localization. Entropy **23**(10), 1244 (2021)
7. Landry, D., Pomerleau, F., Giguere, P.: Cello-3D: Estimating the covariance of ICP in the real world. In: 2019 International Conference on Robotics and Automation (ICRA), pp. 8190–8196. IEEE, Montreal (2019)
8. Zhao, Z., et al.: Efficient and adaptive lidar–visual–inertial odometry for agricultural unmanned ground vehicle. Int. J. Adv. Rob. Syst. **19**(2), 17298806221094924 (2022)
9. Wilbers, D., Merfels, C., Stachniss, C.: Localization with sliding window factor graphs on third-party maps for automated driving. In: 2019 International Conference on Robotics and Automation (ICRA), pp. 5951–5957. IEEE, Montreal (2019)
10. Ding, J., et al.: Refined on-manifold IMU preintegration theory for factor graph optimization based on equivalent rotation vector. IEEE Sens. J. **23**(5), 5200–5219 (2023)
11. Otegui, J., et al.: Evaluation of experimental GNSS and 10-DOF MEMS IMU measurements for train positioning. IEEE Trans. Instrum. Meas. **68**(1), 269–279 (2018)
12. Wei, X., et al.: An improved integrated navigation method with enhanced robustness based on factor graph. Mech. Syst. Signal Process. **155**, 107565 (2021)
13. Wang, A., et al.: SITAN matching algorithm based on adaptive parallel extended Kalman filter. Chin. J. Inertial Technol. **30**(01), 81–88 (2022)

Design of Dual-Rotor Vehicle Controller Based on Auto Disturbance Rejection

Xue Sun[1,2(✉)], Donghui Wang[1,2], Zhengyong Zhan[1,2], and Yuwei Cui[1,2]

[1] AVIC Xi'an Flight Automatic Control Research Institute, Xi'an 710065, China
sxhsr2769@163.com

[2] Aviation Key Laboratory of Science and Technology On Aircraft Control, Xi'an 710065, China

Abstract. Aiming at the characteristics of dual-rotor vehicle, nonlinear, strong coupling and easy to be interfered, a design method of altitude tracking and attitude stabilization using nonlinear active disturbance rejection controller was proposed. The mathematical model of the dual-rotor vehicle was established through dynamic analysis, and the state coupling was regarded as the internal disturbance. The state observer was used to estimate the state and internal and external disturbance of the system in real time, and then the nonlinear feedback was used to compensate the estimated value of the internal and external disturbance of the model, and the state decoupling control of the dual-rotor vehicle was realized. Finally, through the simulation experiment, and compared with the classical PID control method, the experimental results show that the active disturbance rejection controller can realize the altitude tracking and fast and stable attitude control of the dual-rotor vehicle, and has strong anti-interference and robustness.

Keywords: Dual-rotor vehicle · Nonlinear ADRC · State observer · Nonlinear feedback · Decoupling control

1 Introduction

With its unique structure and novel layout, the multi-rotor aircraft has quickly become the focus of the world's universities and scientific research institutions. It has small size, strong maneuverability, less space for takeoff and landing, and still has high maneuverability in the environment with dense obstacles. In the civil field, it is mainly used for high-altitude aerial photography [1], geological exploration and disaster relief, etc. Due to its small size and strong concealment, it can be used for military reconnaissance and battlefield monitoring in the military field [2].

At present, the most common multi-rotor aircraft include four-rotor, six-rotor and eight-rotor, etc. Multi-rotor aircraft mainly adjusts flight attitude and space position by changing rotor speed. However, the multi-rotor aircraft all have disadvantages such as large power consumption and short flight duration [3]. The dual-rotor vehicle, by reducing the number of rotors, not only effectively reduces the power demand during flight, but also makes the aircraft smaller with fewer rotors and further enhances its

Y. Qu et al. (Eds.): ICAUS 2023, LNEE 1176, pp. 11–23, 2024.
https://doi.org/10.1007/978-981-97-1099-7_2

concealability, which can play a good role in search and rescue, monitoring and other special occasions.

While dual-rotor vehicle has advantages, new technical difficulties also appear. Due to its special structure, the system of dual-rotor vehicle is characterized by nonlinear, multi-variable, strong coupling and easy to be interfered [4]. In addition, due to the small size of the dual-rotor vehicle, it is easy to be affected by turbulence in actual flight, which increases the difficulty of control. In order to realize autonomous and stable flight of dual-rotor vehicle in complex environment, the designed controller must have certain anti-interference ability and strong robustness [5].

With the rise of modern control theory, many control methods have come into being. For rotorcraft, the main control methods include classical PID control [6], sliding mode control [7], model predictive control [8], active disturbance rejection control [5], etc. In recent years, domestic and foreign scholars have done a lot of research on the control methods of dual-rotor vehicle, and developed the corresponding model of dual-rotor vehicle. Qimin Zhang et al. analyzed the dynamic model of the dual-rotor and designed the PID controller with attitude stability, which basically met the control requirements of the system, but lacked the altitude control of the aircraft, and the PID controller had poor anti-interference performance [9]. Instead, the team combined with IMU sensors to design improved N-PID controllers, with nonlinear modules placed after them, which improved the stability of dual-rotor vehicle during flight. (source: venturebeat) However, the designed controller has certain robustness and high stability only within the range that the error of the control stable process is close to zero [10].

In view of the special structure of the dual-rotor vehicle, the system has the characteristics of high nonlinear, strong coupling, easy to be disturbed by air flow, and the problems of difficult control in actual flight, this paper based on the nonlinear dynamics model of the dual-rotor vehicle, uses PID control and active disturbance rejection control to complete the design of the dual-rotor vehicle controller, and realizes the altitude tracking and attitude stability control of the aircraft. At the same time, the performance of the two controllers is compared and analyzed by simulation experiment, which verifies the superiority of active disturbance rejection control technology.

2 System Dynamics Model

A dual-rotor vehicle is similar to a four-rotor aircraft in that it generates aerodynamic force through its rotors to provide lift for the aircraft. The same speed and inclination of the front and rear rotors to achieve vertical ascent and descent of the vehicle. The asymmetric rotation of the rotor and the rotation of the rotor axis realize pitch, yaw, roll, forward flight and lateral deviation of the aircraft.

In order to determine the position and attitude of the dual-rotor vehicle in the process of motion, it is necessary to build a model in the ground coordinate system and the body coordinate system, and analyze the conversion relationship between the two coordinate systems. Figure 1 shows the schematic diagram of the ground coordinate system and the body coordinate system.

Euler Angle is used to represent the air attitude of dual-rotor vehicle. Combining the ground coordinate system and the body coordinate system, Euler Angle is defined:

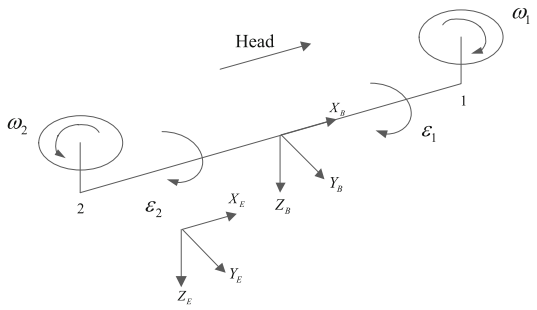

Fig. 1. Schematic diagram of body coordinate system and ground coordinate system

Pitch Angle θ: The Angle between the O_BX_B and the plane $O_EX_EY_E$. Upward is positive.

Yaw Angle ψ: The Angle between the O_BX_B and the plane $O_EX_EZ_E$. The right yaw is positive.

Roll Angle ϕ: The Angle between O_BZ_B and the plane $O_EX_EZ_E$. Right roll turns positive.

Three Euler rotations are required from the ground coordinate system to the body coordinate system, and the rotation matrix is denoted as L_E^B:

$$L_E^B = \begin{bmatrix} \cos\theta\cos\psi & \cos\theta\sin\psi & -\sin\theta \\ \sin\theta\cos\psi\sin\phi - \sin\psi\cos\phi & \sin\theta\sin\psi\sin\phi & \cos\theta\sin\phi \\ \sin\theta\cos\psi\cos\phi + sin\psi sin\phi & \sin\theta\sin\psi\cos\phi - \cos\psi\sin\phi & \cos\theta\cos\phi \end{bmatrix} \tag{1}$$

The rotational angular velocity of the dual-rotor vehicle around the body axis O_BX_B 、O_BY_B 、O_BZ_B axis is $\begin{bmatrix} p & q & r \end{bmatrix}^T$, and the angular velocity of the three Euler angles is $\begin{bmatrix} \dot{\phi} & \dot{\theta} & \dot{\psi} \end{bmatrix}^T$. The relation matrix between the two is as follows:

$$\begin{bmatrix} \dot{\phi} \\ \dot{\theta} \\ \dot{\psi} \end{bmatrix} = \begin{bmatrix} 1 & \tan\theta\sin\phi & \tan\theta\cos\phi \\ 0 & \cos\phi & -\sin\phi \\ 0 & \sin\phi/\cos\theta & \cos\phi/\cos\theta \end{bmatrix} \begin{bmatrix} p \\ q \\ r \end{bmatrix} \tag{2}$$

Dual-rotor vehicle is an underactuated system with six degrees of freedom and four control inputs. Coupling exists between each control variable and the system is highly complex. Therefore, the following assumptions are proposed to simplify the model [11]:

(1) Ignoring the elastic deformation and vibration of the blade, the aircraft is regarded as a rigid body;
(2) Assume that the mass distribution of the aircraft is uniform, the structure is symmetrical, and the geometric center is coincident with the center of gravity;
(3) Regardless of earth rotation, the ground coordinate system is an inertial coordinate system, and the gravity and drag of the aircraft are not affected by external conditions;
(4) The lift generated by the rotor is proportional to the square of the motor speed, $F_i = K_T\omega_i^2, i = 1, 2$;

(5) Aircraft plane symmetry about $O_BX_BZ_B$,

$I_{xy} = I_{yx} = 0, I_{xz} = I_{zx} = 0, I_{yz} = I_{zy} = 0.$

According to the force and torque calculation of the dual-rotor vehicle, the nonlinear model of the system is derived as follows:

$$\begin{cases} \ddot{x} = ((sin\theta cos\psi sin\phi - sin\psi cos\phi)K_T(\omega_1^2 cos\varepsilon_1 + \omega_2^2 cos\varepsilon_2) \\ -(sin\theta cos\psi cos\phi + sin\psi sin\phi)K_T(\omega_1^2 \sin\varepsilon_1 + \omega_2^2 \sin\varepsilon_2))/m \\ \ddot{y} = ((sin\theta sin\psi sin\phi + cos\psi cos\phi)K_T(\omega_1^2 cos\varepsilon_1 + \omega_2^2 cos\varepsilon_2) \\ -(sin\theta sin\psi cos\phi - cos\psi sin\phi)K_T(\omega_1^2 \sin\varepsilon_1 + \omega_2^2 \sin\varepsilon_2))/m \\ \ddot{z} = (\cos\theta \sin\phi K_T(\omega_1^2 cos\varepsilon_1 + \omega_2^2 cos\varepsilon_2) \\ -\cos\theta \cos\psi K_T(\omega_1^2 \sin\varepsilon_1 + \omega_2^2 \sin\varepsilon_2))/m + g \end{cases} \tag{3}$$

$$\begin{cases} I_x\dot{p} = hK_T(\omega_1^2 cos\varepsilon_1 + \omega_2^2 cos\varepsilon_2) - rq(I_z - I_y) \\ I_y\dot{q} = lK_T(\omega_1^2 \sin\varepsilon_1 - \omega_2^2 \sin\varepsilon_2) - rp(I_x - I_z) \\ I_z\dot{r} = hK_T(\omega_1^2 cos\varepsilon_1 - \omega_2^2 cos\varepsilon_2) - pq(I_y - I_x) \end{cases} \tag{4}$$

$$\begin{cases} \dot{\phi} = p + (rcos\phi + qsin\phi)tan\theta \\ \dot{\theta} = q\cos\phi - r\sin\phi \\ \dot{\psi} = (rcos\phi + qsin\phi)/cos\theta \end{cases} \tag{5}$$

where, K_T is the lift coefficient of the rotor; ω_1,ω_2 are the rotational speeds of the front and rear rotor motors, ε_1,ε_2 are the included angles between the axes of the front and rear steering engines and the $O_BX_BY_B$ plane, m is the mass of the dual-rotor vehicle, h is the vertical distance from the center of the rotor to the plane of the body, l is the horizontal distance from the center of the rotor to the center of mass. I_x,I_y,I_z are the moment of inertia of the three axes respectively.

The actual input variables of the dual-rotor vehicle are the rotational speed ω_1,ω_2 of the front and rear motors and the inclination Angle ε_1,ε_2 of the two steering engines. It is complicated to solve the position and attitude of the aircraft directly through the above four control variables. In order to simplify the model, four virtual input variables are defined:

$$U = \begin{bmatrix} U_1 \\ U_2 \\ U_3 \\ U_4 \end{bmatrix} = \begin{bmatrix} K_T(\omega_1^2 sin\varepsilon_1 + \omega_2^2 sin\varepsilon_2) \\ K_T(\omega_1^2 sin\varepsilon_1 - \omega_2^2 sin\varepsilon_2) \\ K_T(\omega_1^2 \cos\varepsilon_1 + \omega_2^2 \cos\varepsilon_2) \\ K_T(\omega_1^2 \cos\varepsilon_1 - \omega_2^2 \cos\varepsilon_2) \end{bmatrix} \tag{6}$$

The nonlinear simplified model of the system can be obtained:

$$\begin{cases} \ddot{x} = (sin\theta cos\psi sin\phi - sin\psi cos\phi)U_3/m - (sin\theta cos\psi cos\phi + sin\psi sin\phi)U_1/m \\ \ddot{y} = (sin\theta sin\psi sin\phi + cos\psi cos\phi)U_3/m - (sin\theta sin\psi cos\phi - cos\psi sin\phi)U_1/m \\ \ddot{z} = \cos\theta \sin\phi U_3/m - \cos\theta \cos\psi U_1/m + g \end{cases} \tag{7}$$

$$\begin{cases} \dot{p} = (hU_3 - rq(I_z - I_y))/I_x \\ \dot{q} = (lU_2 - rp(I_x - I_z))/I_y \\ \dot{r} = (hU_4 - pq(I_y - I_x))/I_z \end{cases} \tag{8}$$

$$\begin{cases} \dot{\phi} = p + (rcos\phi + qsin\phi)tan\theta \\ \dot{\theta} = q\cos\phi - r\sin\phi \\ \dot{\psi} = (rcos\phi + qsin\phi)/cos\theta \end{cases} \tag{9}$$

3 Design of Active Disturbance Rejection Controller

3.1 Principle of Active Disturbance Rejection Controller

Active disturbance rejection control theory was proposed by Han Jingqing in 1988. The core is Tracking Differentiator [12] (Tracking Differentiator, TD), Extended State Observer [13] (Extended State Observer, ESO) and Nonlinear State Error Feedback Law [14] (Nonlinear State Error Feedback Law, NLSEF). Active disturbance rejection controller is robust and has been widely used in aerospace field. Active disturbance rejection control retains the advantage that PID control does not depend on the model. Traditional PID control cannot estimate and compensate unknown disturbance, and its anti-interference ability is weak. However, active disturbance rejection control can estimate the internal uncertainties of the system and external environmental interference in real time, and all disturbances are collectively referred to as "total disturbance".

Taking the second-order control object as an example, the structure of the second-order active disturbance rejection controller is shown in Fig. 2.

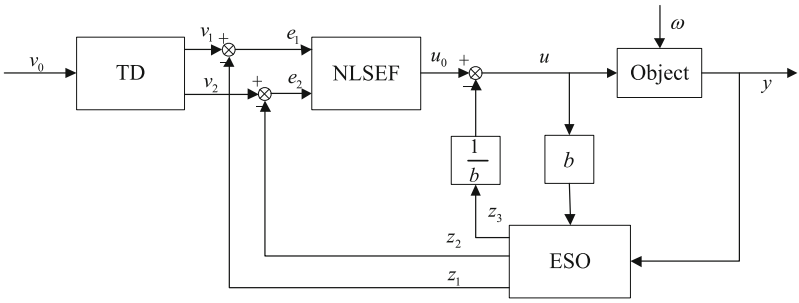

Fig. 2. Block diagram of second order active disturbance rejection controller

3.2 Design of Active Disturbance Rejection Controller

According to the dual-rotor system dynamics model established in the previous paper, the three channels of roll, pitch and yaw of the aircraft are coupled with each other, and the active disturbance rejection controller regards the coupling between attitude as the uncertain interference inside the system, and the disturbance caused by wind field environmental interference and gyroscopic effect in the external environment is regarded as the total disturbance of the channel. After that, each channel independently uses the extended state observer for real-time observation and estimation. Thus decoupling

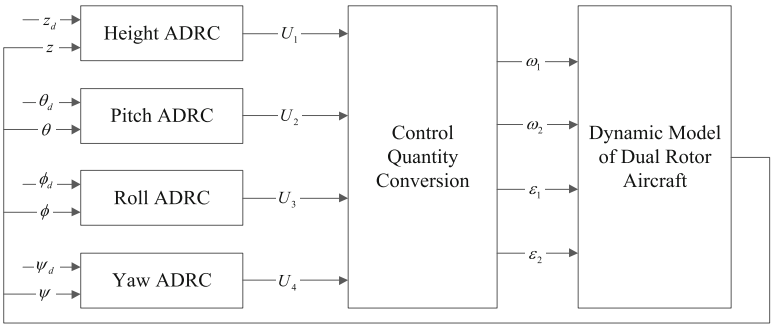

Fig. 3. Active disturbance rejection controller structure diagram

control is realized. The structure of active disturbance rejection control loop of the whole system is shown in Fig. 3, which is divided into four independent loops: height control loop, roll control loop, pitch control loop and yaw control loop.

Through the above analysis, Eqs. (7), (8) and (9) can be rewritten into the following formula:

$$\begin{cases} \ddot{z} = f_1(z, \dot{z}) + \omega_1 + b_1 U_1 \\ \ddot{\theta} = f_2(\theta, \dot{\theta}, \phi, \dot{\phi}, \psi, \dot{\psi}) + \omega_2 + b_2 U_2 \\ \ddot{\phi} = f_3(\theta, \dot{\theta}, \phi, \dot{\phi}, \psi, \dot{\psi}) + \omega_3 + b_3 U_3 \\ \ddot{\psi} = f_4(\theta, \dot{\theta}, \phi, \dot{\phi}, \psi, \dot{\psi}) + \omega_4 + b_4 U_4 \end{cases} \tag{10}$$

where, $f_i(\bullet)$ is the coupling or uncertain disturbance within the system, ω_i is the interference of external environment, $b_1 \approx -\frac{1}{m}, b_2 \approx \frac{l}{I_y}, b_3 \approx \frac{h}{I_x}, b_4 \approx \frac{l}{I_z}$.

According to Eq. (10), the control object is a second-order nonlinear uncertain object, so the second-order active disturbance rejection controller needs to be designed. The design of active disturbance rejection controller consists of three parts, TD, ESO and NLSEF. Taking pitch channel as an example, the active disturbance rejection control algorithm in discrete form is given below:

Controlled object: $\ddot{\theta} = f(\theta, \dot{\theta}, \phi, \dot{\phi}, \psi, \dot{\psi}) + \omega + bu, \quad y = \theta.$

(1) Discrete Tracking Differentiator

$$\begin{cases} v_1(k+1) = v_1(k) + Tv_2(k) \\ v_2(k+1) = v_2(k) + Tfst(v_1(k) - \theta_d(k), v_2(k), r, h) \end{cases} \tag{11}$$

where:

$$fst(x_1, x_2, r, h) = \begin{cases} -ra/d\ , & a \le d_0 \\ -rsign(a)\ , & a > d_0 \end{cases} \tag{12}$$

$$\begin{cases} d = rh \\ d_0 = dh \\ y = x_1 + hx_2 \\ a_0 = \sqrt{d^2 + 8r|y|} \end{cases} \tag{13}$$

$$a = \begin{cases} x_2 + \frac{(a_0 - d)}{2} sign(y) \ , \ |y| > d_0 \\ x_2 + \frac{y}{h} \ , \ |y| \leq d_0 \end{cases} \tag{14}$$

where, θ_d is the expected value of pitch Angle; r is the speed factor, which determines the tracking speed; h is the filtering factor, which plays a filtering role on noise; h and r parameters are adjustable. The tracking differentiator overcomes the influence of noise signal and eliminates the chatter phenomenon which is easy to appear at the origin.

(2) Discrete Extended State Observer

$$\begin{aligned} &\varepsilon = z_1(k) - y(k) \\ &\begin{cases} z_1(k+1) = z_1(k) + T(z_2(k) - \beta_1 \varepsilon_1) \\ z_2(k+1) = z_2(k) + T(z_3(k) \\ -\beta_2 fal(\varepsilon, \alpha_1, \delta) + bu(k)) \\ z_3(k+1) = z_3(k) - T\beta_3 fal(\varepsilon, \alpha_2, \delta) \end{cases} \end{aligned} \tag{15}$$

where:

$$fal(\varepsilon, \alpha, \delta) = \begin{cases} |\varepsilon|^{\alpha} sign(\varepsilon) \ , \ |\varepsilon| > \delta, \\ \varepsilon / \delta^{1-\alpha} \ , \ |\varepsilon| \leq \delta, \end{cases} \quad \delta > 0 \tag{16}$$

where b is the control input scaling coefficient, u and y are the input and output signals of the system, $\beta_1, \beta_2, \beta_3$ is the gain coefficient of the observer, which is greater than zero, $0 < \alpha_1 < \alpha_2 < 1$, δ determines the width of the linear interval, and increasing the linear interval can avoid the oscillation of the *fal* function near the origin.

(3) Discrete Nonlinear Error Feedback Control Law

$$\begin{cases} e_1 = v_1(k) - z_1(k) \\ e_2 = v_2(k) - z_2(k) \\ u_0(k) = k_1 fal(e_1, \alpha_1, \delta) + k_2 fal(e_2 \alpha_2, \delta) \\ u(k) = u_0(k) - \frac{z_3(k)}{b} \end{cases} \tag{17}$$

where,k_1, k_2 is the controller gain coefficient, in $\alpha < 1$, the *fal* function has the characteristics of large error and small gain, and small error and large gain to avoid control saturation caused by excessive error of the controller. δ transforms the *fal* function into a linear continuous function near the origin to avoid high-frequency flutter of the *fal* function near the origin [15].

It can be drawn from the pitch Angle ADRC controller that the controller itself does not need the specific model of the controlled object, nor does it need to analyze the stability of the controller for the control object. It only needs to select the appropriate parameters to realize the attitude and height stability control. The other controllers are designed similarly to the ADRC controller for pitch Angle.

4 Simulation Experiment and Result Analysis

4.1 Simulation Experiment of ADRC Controller

According to the active disturbance rejection control algorithm designed above, the active disturbance rejection controller is built in the MATLAB/Simulink environment. The active disturbance rejection controllers of different channels are similar.

The control period T = 0.01s is selected, and the parameters are tuned according to the parameter selection principle given in literature [16]. After many simulation experiments, the simulation parameters of ADRC are determined as shown in Table 1.

Table 1. ADRC simulation parameters

	parameter	Roll controller	Pitch controller	Yaw controller	Height controller
TD	r	140	100	160	140
	h	0.05	0.05	0.05	0.05
ESO	α_1	0.5	0.5	0.5	0.5
	α_2	0.25	0.25	0.25	0.25
	β_1	100	100	100	100
	β_2	200	200	200	200
	β_3	300	300	300	300
	δ_1	0.0025	0.0025	0.0025	0.0025
	b	1	1	1	1
NLSEF	α_1	0.7	0.7	0.7	0.7
	α_2	0.95	0.95	0.95	0.95
	δ_2	0.0025	0.0025	0.0025	0.0025
	k_1	200	200	220	250
	k_2	180	180	190	245

According to the ADRC parameters in Table 1, the simulation experiment is carried out, and the initial height of the dual-rotor vehicle is set to $z = 0$m, The initial attitude angle $\phi = 0$rad, $\theta = 0$rad, $\psi = 0$rad, The system sampling period is T = 0.01s, and the control goal is to make the aircraft achieve the height $z = 5$m, The attitude angle $\phi = 0.4$rad, $\theta = 0.4$rad, $\psi = 0.4$rad, The simulation results are shown in Fig. 4.

The performance indicators of the active disturbance rejection controller can be obtained through the above simulation, as shown in Table 2.

According to the simulation results shown in Fig. 4, the active disturbance rejection controller has good effect, short adjustment time, small overshoot, good system stability, and is not prone to oscillation. The steady-state error is almost 0. At the same time, the attitude stability can be achieved within 1s, and the target altitude can be reached within 1.5s. Therefore, the active disturbance rejection controller can meet expectations and achieve stability control of the dual-rotor vehicle.

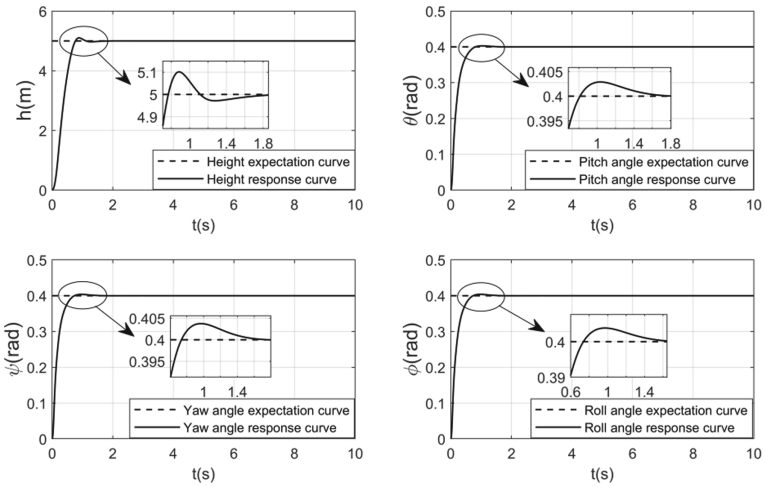

Fig. 4. Response curve of active disturbance rejection controller

Table 2. Performance index

	t_s/s	$\sigma\%$
h	1.11	2.02
θ	0.54	0.675
ψ	0.68	0.94
ϕ	0.66	0.95

4.2 Comparison with PID Controller Simulation Experiment

Altitude and Attitude Tracking Experiment

In order to verify the superiority of active disturbance rejection control, this paper compares the classical PID controller with the active disturbance rejection controller by simulation. The initial state and expected state of the aircraft are the same as in Sect. 4.1. In the case of no external interference, the simulation results are shown in Fig. 5.

In the case of no interference, it can be seen from Fig. 5 that the adjustment time of PID controller is about 2s and the overshoot is about 10%, which is significantly higher than that of the active disturbance rejection controller. The reason is that the active disturbance rejection control has a tracking differential, which can quickly track the signal, and it can respond quickly to meet the expected value while ensuring the low overshoot of the system, thus resolving the contradiction between the overshoot and the adjustment time. Therefore, dual-rotor vehicle is more suitable for active disturbance rejection controller in the case of no interference.

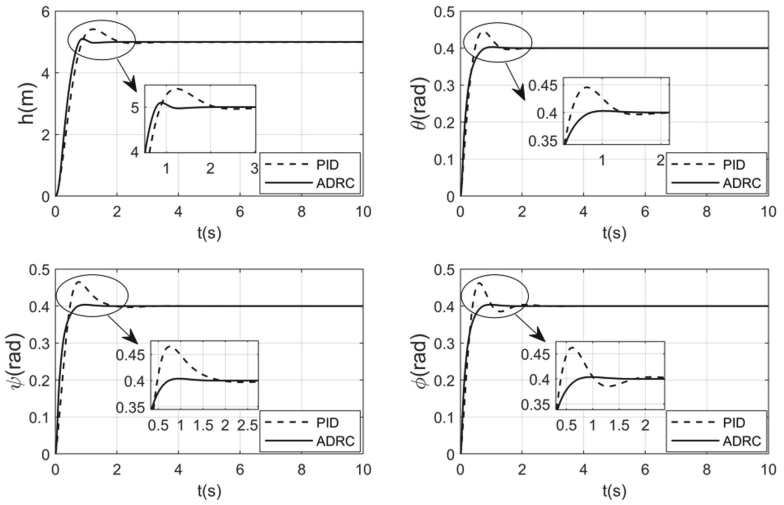

Fig. 5. Comparison of PID and active disturbance rejection control responses

Disturbance Experiment

The aircraft will be affected by various noises and external disturbances in actual flight. The sensor noise is simulated by applying Gaussian white noise with variance of 10 to the altitude and attitude Angle. At the same time, rectangular wave with amplitude of 1 and pulse width of 0.5s is applied to the velocity in the altitude z direction, pitch, yaw and roll angular velocity respectively at 5s to simulate the external disturbance. Test the anti-interference of the controller. The comparison of simulation results between PID control and active disturbance rejection control can be obtained, as shown in Fig. 6.

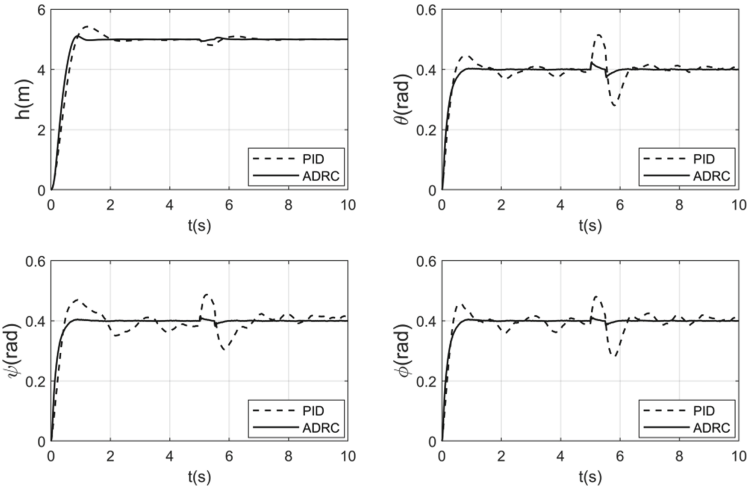

Fig. 6. Comparison of anti-interference performance between PID and auto-disturbance rejection